J. Fluid Mech. (2015), *vol.* 772, *pp.* 756–783. © Cambridge University Press 2015
doi:10.1017/jfm.2015.227

Amplitude and frequency modulation of the small scales in a jet

D. Fiscaletti[1,†], B. Ganapathisubramani[2] and G. E. Elsinga[1]

[1]Laboratory for Aero and Hydrodynamics, Department of Mechanical, Maritime, and Materials Engineering, Delft University of Technology, Leeghwaterstraat 21, 2628 CA, Delft, The Netherlands

[2]Aerodynamics and Flight Mechanics Research Group, University of Southampton, Southampton SO17 1BJ, UK

(Received 17 December 2014; revised 3 March 2015; accepted 15 April 2015; first published online 8 May 2015)

The present study is an experimental investigation of the relationship between the large- and small-scale motions in the far field of an air jet at high Reynolds number. In the first part of our investigation, the analysis is based on time series of hot-wire anemometry (HWA), which are converted into space series after applying the Taylor hypothesis. By using a spectral filter, two signals are constructed, one representative of the large-scale motions ($2\lambda_T - L$, where λ_T is the Taylor length scale, and L is the integral length scale) and the other representative of the small-scale motions (1.5–5η, where η is the Kolmogorov length scale). The small-scale signal is found to be modulated both in amplitude and in frequency by the energy-containing scales in an analogous way, both at the centreline and around the centreline. In particular, for positive fluctuations of the large-scale signal, the small-scale signal is locally stronger in amplitude (amplitude modulation), and it locally exhibits a higher number of local maxima and minima (frequency modulation). The extent of this modulation is quantified based on the strength of the large-scale fluctuations. The response of the small-scale motions to amplitude modulation can be considered instantaneous, being on the order of one Kolmogorov time scale. In the second part of our investigation we use long-range μPIV to study the behaviour of the small-scale motions in relation to their position in either high-speed or low-speed regions of the flow. The spatially resolved velocity vector fields allow us to quantify amplitude modulation directly in physical space. From this direct estimation in physical space, amplitude modulation is only 25 % of the value measured from HWA. The remaining 75 % comes from the fixed spectral band filter used to obtain the large- and small-scale signals, which does not consider the local convection velocity. A very similar overestimation of amplitude modulation when quantified in the time-frame is also obtained analytically. Furthermore, the size of the structures of intense vorticity does not change significantly in relation to the large-scale velocity fluctuation, meaning that there is no significant spatial frequency modulation. The remaining amplitude modulation in space can be explained as a statistical coupling between the strength of the structures of vorticity and their preferential location inside

† Email address for correspondence: d.fiscaletti@tudelft.nl

https://doi.org/10.1017/jfm.2015.227 Published online by Cambridge University Press

large-scale high-velocity regions. Finally, the implications that the present findings have on amplitude and frequency modulation in turbulent boundary layers (TBLs) are discussed.

Key words: jets, wakes/jets

1. Introduction

The interaction between the different scales of turbulence has been the subject of a great many investigations in the past few years. According to the classical theory of turbulence, turbulent kinetic energy is produced at large scales, and it is then transferred on average to ever smaller scales in an inviscid process, before being dissipated into heat (Richardson 1926; Pope 2000). The classical theory of turbulence considers the mechanism of energy transfer to be universal (Pope 2000). Furthermore, some properties of the small scales of turbulence have been observed to be independent of the flow under investigation; see Sreenivasan & Antonia (1997), Elsinga & Marusic (2010), Wei *et al.* (2014), among others. Despite the universality of various important features of turbulence, several works have reported that in turbulent boundary layers (TBLs) the large-scale motions appear to interact with the viscous scales in a different way depending on the distance from the wall (Hutchins & Marusic 2007*a*; Chung & McKeon 2010; Mathis, Hutchins & Marusic 2009; Ganapathisubramani *et al.* 2012). Although such interaction between the large-scale and small-scale motions has lately aroused deep interest, shear flows other than boundary layers have scarcely been tackled in the literature. Only a mixing layer has been studied so far (Buxton 2011; Buxton & Ganapathisubramani 2014).

In turbulence, the clear separation of the scales is achieved in flows at high Reynolds number. However, the ratio between the large scales and the small scales of turbulence (dynamic range) is almost proportional to the Reynolds number of the flow, thus making the simultaneous tracking of the entire range of scales difficult. For these reasons, the recent works on scale interaction in TBLs at high Reynolds numbers rely on HWA data, as it offers a large temporal dynamic range. Some early indications of top-down interaction in the boundary layer were found in the work by Hutchins & Marusic (2007*b*), who noticed that the very large-scale motions influence the near-wall turbulence, which was originally regarded as an independent region of the TBL (Jiménez & Pinelli 1999; Schoppa & Hussain 2002). Two years later, these qualitative observations led Mathis *et al.* (2009) to quantify the large-scale modulation of the small scales in a TBL at high Reynolds number. The authors applied a procedure similar to Bandyopadhyay & Hussain (1984). They reconstructed two signals representative of the large- and small-scale motions (named large-scale and small-scale signal, respectively) by applying a spectral filter on time series from HWA. The Taylor hypothesis of frozen turbulence (Taylor 1938) made it possible to create an analogy between the length scales of turbulence and the frequency content of the signal. The small-scale signal was then Hilbert-transformed and low-pass filtered, in order to create a signal representative of the local small-scale activity. It can be thought of as the filtered envelope of the small-scale signal. The correlation coefficients between this signal and the large-scale signal were computed at different distances from the wall. This procedure made it possible to retrieve an estimate of the local degree of amplitude modulation. It was found that the near-wall region

https://doi.org/10.1017/jfm.2015.227 Published online by Cambridge University Press

is characterized by a positive top-down interaction, i.e. positive fluctuations of the large-scale signal induce a local increment to the amplitude of the small-scale signal. On the other hand, further from the wall, a phase reversal was reported (see also Chung & McKeon 2010; Jacobi & McKeon 2013), with the small-scale signal being statistically less intense for positive large-scale fluctuations.

However, Schlatter & Örlü (2010) found that the correlation coefficient between the large-scale signal and the envelope of the small-scale signal is not an independent tool to quantify the degree of amplitude modulation. It was shown that a synthetic signal characterized by the same skewness as the original signal also has the same value for the correlation coefficient. The authors therefore invoked a note of caution. Bernardini & Pirozzoli (2011) suggested the use of two-point correlation to overcome this limitation, and proved that the physical phenomenon observed by Mathis *et al.* (2009) is not an artifact of the mathematical tool used in that quantification. Later, Mathis *et al.* (2011) decomposed the skewness factor into contributions from large- and small-scale signals. They found that one of the terms constituting the skewness factor closely resembles the correlation coefficient used to quantify amplitude modulation. In particular, that term becomes more and more similar to the skewness factor of the signal for increasing the Reynolds number of the flow, which explains the analogy between skewness factor and correlation coefficient. Recently, Ganapathisubramani *et al.* (2012) showed that the small-scale amplitude grows with increasing values of the large-scale fluctuation in the near-wall region, whereas in the outer region the small-scale amplitude decreases with increasing large-scale fluctuation. In particular, the small-scale signal is more amplitude-modulated when the strength of the large-scale fluctuation increases. Furthermore, a method based on the number of occurrences of local maxima and minima of the signal made it possible to explore effects of frequency modulation. The frequency of the small-scale signal was reported to be higher for positive large-scale fluctuations and lower for negative large-scale fluctuations. This evidence is stronger in the near-wall region, and it becomes weaker at a distance from the wall larger than 100 wall units. In that work, the authors hypothesized that both the frequency and amplitude modulation are the result of a change in the local Reynolds number of the flow.

The top-down interaction between the scales of turbulence has so far been studied very intensively in boundary layers, with the further aim of controlling the activity of the viscous scales in the near-wall region (Marusic, Mathis & Hutchins 2010; Mathis, Hutchins & Marusic 2011). The large-scale modulation of the small scale has barely been explored in free shear flows. An extensive analysis of the phenomenon in different flows was performed by Bandyopadhyay & Hussain (1984), who examined a wake, a mixing layer, and a jet. They found that a wake and a jet behave in a similar way to the near-wall region of a TBL, i.e. the small-scale signal exhibits a stronger amplitude for positive fluctuations of the large-scale signal, independently of the radial location. The mixing layer, on the other hand, presents a phase reversal between large- and small-scale signals analogous to the outer region of a TBL. In the present study, the nature of the interaction between large- and small-scale velocity fluctuations is examined in a turbulent jet at high Reynolds number. The mean shear vanishes at the centreline of a far-field jet, which represents an important difference with respect to boundary layers and mixing layers.

The far field of a jet is characterized by isotropy of the small scales on average (Pope 2000; Ganapathisubramani, Lakshminarasimhan & Clemens 2008; Cardesa *et al.* 2013). Nevertheless, the small-scale motions were observed to be highly intermittent locally and inhomogeneous in a large number of works (She, Jackson & Orszag 1990;

https://doi.org/10.1017/jfm.2015.227 Published online by Cambridge University Press

Shen & Warhaft 2000; Ishihara, Toshiyuki & Kaneda 2009; Fiscaletti, Westerweel & Elsinga 2014, among others). This inhomogeneity reinforces with increase in the Reynolds number of the flow. Moreover, the small-scale motions were observed to organize themselves into coherent structures. For example, intense vorticity appears in the shape of vortex tubes (Siggia 1981; Ashurst *et al.* 1987; Vincent & Meneguzzi 1991), called 'worms' after the work by Jiménez *et al.* (1993). These worms have a characteristic diameter of approximately 10η over a very large range of Reynolds numbers based on the Taylor scale (Kaneda & Ishihara 2006; Ishihara, Kaneda & Hunt 2013; Fiscaletti *et al.* 2014), whereas their length was proposed to scale with the integral length scale of the flow (Jiménez *et al.* 1993; Ganapathisubramani *et al.* 2008). Consistent with the high intermittency of turbulence at the small-scale level, the worm-like structures were observed to cluster in regions of flow of intense shear (Worth & Nickels 2011; Ishihara *et al.* 2013), and high rate of dissipation (Vincent & Meneguzzi 1994; Chacin & Cantwell 2000; Ganapathisubramani *et al.* 2008). On the other hand, with the intense vortices gathering in clusters, large portions of the flow are characterized by very low vorticity.

The present study aims at a detailed assessment of amplitude and frequency modulation of the small scales in a jet at high Reynolds number. In the first part of the investigation, the scale interaction is examined with HWA. The use of HWA, however, requires application of the Taylor hypothesis of frozen turbulence if length scales are to be considered, which has already been reported in the past to be a considerable source of bias (Zaman & Hussain 1981; del Álamo & Jiménez 2009). For this reason, the phenomenon is studied in the second part with long-range μPIV. In this way, amplitude and spatial frequency modulation can be quantified without any need for conversion of the signal from the time domain to the spatial domain typical of HWA. This will be shown to greatly affect the level of amplitude modulation. Moreover, long-range μPIV allows exploration of the relation between amplitude modulation and the coherent structures. Finally, we speculate on the implications of these findings for TBL flows.

2. Experiments

The air jet under investigation issued from a round nozzle with an exit diameter of $D = 8$ mm. The flow velocity at the nozzle exit is 125 m s^{-1}, as established in a separate measurement with a Pitot tube of 1.5 mm in diameter. The non-dimensional numbers at the nozzle can be estimated: Reynolds number $Re = 6.6 \times 10^4$ and Mach number $Ma = 0.37$. The inlet chamber upstream of the nozzle consists of a diffuser with an angle of about 22°, followed by a series of five fine irregular mesh screens with an average mesh size of about 1 mm^2, intended to reduce the size of the largest scales present in the flow. A 25:1 contraction is followed by a round nozzle, whose edges are slightly chamfered. Further details of the settling chamber and the shape of the nozzle can be found in Slot *et al.* (2009). Two different techniques were used to measure the jet flow: HWA and long-range microscopic particle image velocimetry (long-range μPIV).

2.1. *Hot-wire anemometry*

The measurements were performed at a downstream distance of 70 nozzle diameters from the nozzle exit, at two different radial locations, namely at the centreline and at 0.2 $r_{1/2}$, where $r_{1/2}$ is the jet's half-width. At this stage, the turbulence of the flow is fully developed, and the jet is characterized by its typical self-similar

https://doi.org/10.1017/jfm.2015.227 Published online by Cambridge University Press

Jet exit diameter, D	8 mm
Jet exit velocity	124.8 m s^{-1}
Reynolds number based on the jet exit conditions	6.6×10^4
Spreading rate, $S = \mathrm{d}r_{1/2}(x)/\mathrm{d}x$	0.096
Decay rate of the centreline velocity, $B = U_0(x)(x - x_0)/(U_J D)$	5.6
Measurement location, x/D	70
Centreline velocity U_c $(x/D = 70)$	10.56 m s^{-1}
Jet half-width, $r_{1/2}$ $(x/D = 70)$	52.2 mm

TABLE 1. Macroscopic characteristics of the jet flow as estimated from HWA and Pitot tube measurements.

behaviour, as demonstrated in Fiscaletti *et al.* (2014). The sensor, a tungsten Dantec 55P11, was operated in constant temperature mode, with an overheat ratio of 0.7. In this way, its temperature was kept approximately constant at 220 °C throughout the entire measurement process. The length of the sensor was 1.25 mm and its diameter was 5 μm, equivalent to 23η and 0.09η respectively, where η is the Kolmogorov length scale of the flow at the measurement location. The feedback control of the wire temperature was established through a Dantec Dynamics 56C17 CTA Bridge. Data were acquired at a frequency of 200 kHz, over a time of 4 s per run (8×10^5 samples). An estimate of the dissipation rate in jets is provided using the approximation (Panchapakesan & Lumley 1993)

$$\varepsilon \approx 0.015 \frac{U_c^3}{r_{1/2}}, \tag{2.1}$$

where U_c is the centreline velocity and $r_{1/2}$ is the jet's half-width. Based on the dissipation rate at the above-mentioned measurement location, the size of the Kolmogorov scale η is estimated to be 57 μm, which corresponds to a frequency of 30 kHz at the jet centreline when employing Taylor's hypothesis. Since, for frequencies higher than 22 kHz, the measurement noise dramatically affects the signal, a low-pass filtering at this cut-off frequency had to be applied. As a consequence, the minimum size of the eddies that the measurement can resolve is estimated to be 90 μm, corresponding to about 1.5 Kolmogorov length scales. Moreover, an estimate of the Taylor microscale λ_T was obtained from the expression (Taylor 1935)

$$\lambda_T = u' \sqrt{15 \frac{\nu}{\varepsilon}}, \tag{2.2}$$

where u' is the root mean square (r.m.s.) of the axial velocity. Moreover, the integral length scale of the flow (L) can be estimated by

$$L \sim \eta \, Re^{3/4}. \tag{2.3}$$

From the calculation, the Taylor microscale λ_T is 2.19 mm, and the integral length scale of the flow L is 43 mm. The Reynolds number based on the Taylor microscale (Re_λ) was estimated to be 367. Table 1 provides a summary of the macroscopic characteristics of the jet flow.

https://doi.org/10.1017/jfm.2015.227 Published online by Cambridge University Press

2.2. *Long-range μPIV*

The PIV measurement was performed at the same downstream distance of 70 nozzle diameters from the nozzle exit, in proximity to the centreline. The measurement plane was parallel to the axis of the jet. A detailed description of the experiment and its validation based on the main statistical properties of the turbulence are given in Fiscaletti *et al.* (2014). Here we only give a brief overview of the main characteristics of the PIV system. The long-range microscope used in the μPIV system is the Questar QM-1, with a magnification factor of 2.5, and with a working distance of 560 mm. The working distance is more than an order of magnitude higher than the jet's half-width at the measurement location (52.2 mm), which is deemed sufficient to avoid any perturbative effect on the flow.

As seeding tracers, 1 μm DEHS particles (Di(2-ethylhexyl) sebacate, sebacic acid) generated from a Laskin nozzle were used. The response time of this seeding is about two orders of magnitude lower than the Kolmogorov time scale, so that the velocity fluctuations in the flow can be tracked accurately.

A total of 11 000 image pairs were collected at an acquisition frequency of 5 Hz. The dataset of image pairs was processed through a cross-correlation algorithm, implemented in the software DaVis by LaVision. A two-pass refinement of the grid was adopted, with a final interrogation window of 64×64 pixels, and a 50 % window overlap. The size of the interrogation window was 160 μm, which corresponds to 2.9 Kolmogorov length scales at the measurement location. The thickness of the light sheet was almost equal in size (180 μm). The field of view was 3.43×2.60 mm, equivalent to $1.68\lambda_T \times 1.26\lambda_T$, where λ_T is the Taylor length scale as derived from the μPIV data. A time delay of 3 μs was chosen between the first and second laser pulses, yielding an average particle displacement of 11.8 pixels, which corresponds to 9.78 m s^{-1}. The flow characteristics as estimated from μPIV are comparable to those from HWA, and they can be found in table 4 of Fiscaletti *et al.* (2014). The Taylor and Kolmogorov length scales appearing in the non-dimensionalization of physical quantities computed from μPIV data were estimated from μPIV data. The coordinate system x_i and corresponding velocity components u_i for the μPIV dataset are defined as follows: subscripts 1 and 2 represent the axial and radial directions respectively; subscript 3 indicates the direction perpendicular to the measurement plane.

3. Methods for scale separation and coherent structures identification

In this work we address the amplitude and frequency modulation of the small scales of turbulence by the large scales. We rely on the present datasets from both HWA and long-range μPIV. In order to extract large- and small-scale information from both measurement techniques a further treatment of the data is required, which is described next.

3.1. *The filtering of the HWA data*

Figure 1 shows the velocity power spectrum. The $-5/3$ slope in the inertial range of the energy cascade develops over two decades. This demonstrates the highly turbulent nature of the flow, and the clear separation of the large scales and the small scales. In figure 1 we present a low-frequency and high-frequency band, which are taken to be representative of the large-scale signal and the small-scale signal, respectively. In particular, the low-frequency signal is associated with length scales between $2\lambda_T$ and L, whereas the high-frequency signal is associated with length scales between 1.5η

https://doi.org/10.1017/jfm.2015.227 Published online by Cambridge University Press

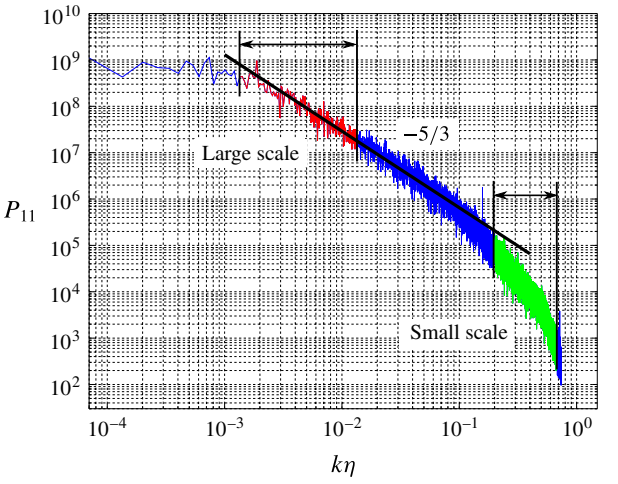

FIGURE 1. (Colour online) Velocity power spectrum of a hot-wire signal taken at the jet centreline, at a downstream distance of 70 nozzle diameters.

and 5η. The velocity is band-pass filtered in the frequency domain, and the frequency components not belonging to the frequency band of interest are set to zero. The new small-scale and large-scale velocity signals are then obtained by applying the inverse fast Fourier transform.

3.2. *The processing of the long-range μPIV data*

In the μPIV measurement, the field of view ($1.68\lambda_T \times 1.26\lambda_T$) is not large enough to fully capture the large scales of turbulence, as defined above for HWA. Therefore the fluctuating axial velocity component averaged over the field of view was considered as the instantaneous local large-scale velocity fluctuation instead. The vector spacing in the μPIV measurement is 1.5η, which is also the size of the smallest eddies that can be resolved with HWA, under the hypothesis of frozen turbulence.

Furthermore, taking advantage of the planar velocity data we analysed the link between the intense vortices or intense dissipation, and the strength of the local large-scale fluctuation. In this analysis the intense dissipation, vorticity and vortical motion are considered to be associated with (or representative of) the small scales of motion. In this section we illustrate the criterion adopted for the detection of the vortices, and for locating their centres. The criterion uses the imaginary part of the eigenvalues of the reduced velocity gradient tensor (VGT), λ_{ci}, where non-zero values indicate a local swirling motion. It is therefore known as the λ_{ci}-criterion, or swirling strength, and it was first proposed by Zhou *et al.* (1999). If λ_{ci} is higher than a certain threshold, a vortex is said to be detected. A threshold value for λ_{ci} ($\lambda_{ci,thr}$) was determined as a multiple of the r.m.s. of λ_{ci}, computed on the dataset where λ_{ci} was non-zero. A vortex is detected if either one point or cluster of multiple points was characterized by

$$\lambda_{ci} > K\,\lambda_{ci,rms}, \tag{3.1}$$

where K is a constant. In order to determine the subgrid position of the centre of each vortex, we computed the centroid of the λ_{ci} distribution within the vortex core.

https://doi.org/10.1017/jfm.2015.227 Published online by Cambridge University Press

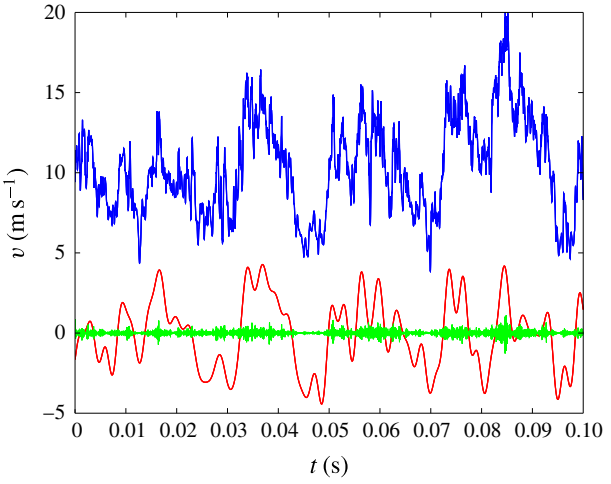

FIGURE 2. (Colour online) Sample from the velocity signal (top) with the corresponding small-scale and large-scale components (bottom).

The convection velocity of a vortex could also be estimated. As an initial approximation, the fluid velocity at the centroid of a vortex can be considered as the convection velocity of that vortex, V.

Furthermore, we will analyse the behaviour of the regions of intense dissipation, with a particular focus on their convection velocities, and their rate of occurrence. The estimate of the local turbulent dissipation rate stemmed from

$$\varepsilon = 2\nu \left(\boldsymbol{A}(1,1)^2 + 2 \left(\frac{\boldsymbol{A}(2,1) + \boldsymbol{A}(1,2)}{2} \right)^2 + \boldsymbol{A}(2,2)^2 \right), \tag{3.2}$$

where $\boldsymbol{A}$ is the reduced (two-dimensional) VGT in a point. A region of intense dissipation is detected if either one point or a cluster of multiple points was characterized by:

$$\varepsilon > K_\varepsilon \, \varepsilon_{rms} \tag{3.3}$$

where K_ε is a constant. Analogous to the intense vortices, the subgrid position of the centre of each region of intense dissipation was identified by calculating the centroid of the ε distribution within the points belonging to the region of intense dissipation. In the following, we refer to convection velocity of a region of intense dissipation V_ε as the axial flow velocity at the centre of the dissipation structure.

4. Amplitude modulation

In figure 2, part of the raw velocity signal (top) is shown, with the corresponding large-scale signal and small-scale signal content (bottom). It appears that the small scales are affected by the large-scale motions. When the large-scale fluctuation is positive the small-scale fluctuations are typically more intense. The large scales thus have a role in modulating the amplitude of the dissipative scales, similar to the observations of Hutchins & Marusic (2007*b*) in the near-wall region. This trend is more evident in figure 3, where the probability density functions (p.d.f.s) of the small-scale velocity fluctuations are presented, conditioned on the large positive and

https://doi.org/10.1017/jfm.2015.227 Published online by Cambridge University Press

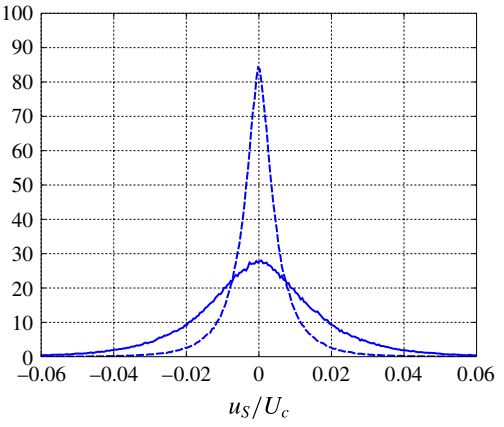

FIGURE 3. (Colour online) Probability density function of the small-scale fluctuations, conditioned on the large positive (continuous line) and large negative (dashed line) fluctuations of the large-scale signal.

large negative fluctuations in the corresponding large-scale signal. The threshold of the large-scale fluctuation was taken to be its r.m.s. value. The variance of the p.d.f. conditioned on the positive fluctuations of the large-scale signal is clearly higher than the variance for the negative large-scale fluctuations: this demonstrates that the sign of the large-scale fluctuations has a modulating effect on the small-scale turbulent activity.

Nevertheless, the variance of the conditional p.d.f. does not provide a detailed description of the relation between the strength of the large-scale signal and the amplitude modulation of the small-scale motions. Hence, a procedure similar to that detailed in Ganapathisubramani *et al.* (2012) was applied to the present experimental dataset. In the following, we let u_L^* denote the fluctuations of the large-scale signal non-dimensionalized by the average centreline velocity U_c ($u_L^* = u_L/U_c$). The aforementioned procedure consists of the following steps.

(i) Equally spaced u_L^* bins were created, with a spacing of 0.05 ranging from $u_L^* = -0.4$ to $u_L^* = 0.4$. A bin spacing of 0.05 was chosen as a balance between the bin size and the number of samples within each bin. With such a size, the minimum amount of samples falling within each bin was larger than 1000.

(ii) Each large-scale sample is associated with a small-scale sample at the same instant in time.

(iii) The associated sample of the small-scale signal was included in a group, corresponding to one of the u_L^* bins, effectively creating an independent new small-scale velocity series for each u_L^* bin.

(iv) The r.m.s. of the samples contained in each group was then computed, and this small-scale r.m.s. represents the amplitude of the small scales conditioned on the strength of the respective large-scale signal, σ_{u_L}. The r.m.s. was non-dimensionalized by the r.m.s. of the entire small-scale fluctuations at the centreline σ_c, and therefore $\sigma_{u_L}^* = \sigma_{u_L}/\sigma_c$.

The analysis was conducted for datasets from two different radial positions, namely at the centreline and at 0.2 non-dimensional radii. Figure 4 shows the result of this procedure for the two different radial locations. The amplitude modulation

https://doi.org/10.1017/jfm.2015.227 Published online by Cambridge University Press

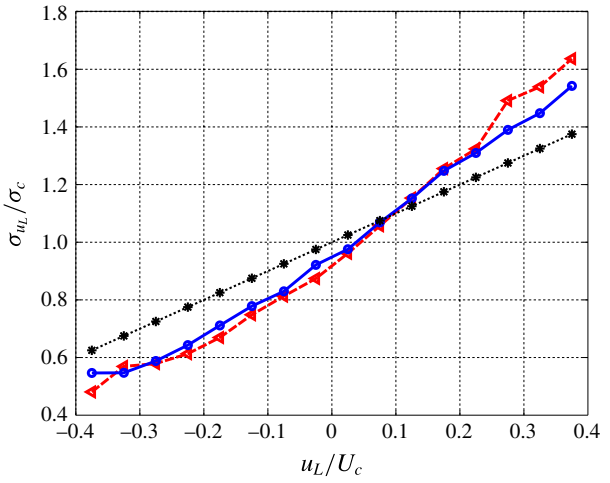

FIGURE 4. (Colour online) Root mean square of the p.d.f. of the small-scale signal $\sigma^*_{u_L} = \sigma_{u_L}/\sigma_c$, conditioned on the fluctuations of the large-scale signal u_L, at the centreline position (continuous line, ○), and at 0.2 non-dimensional radii (dashed line, ◁). A dotted line (∗) has been added, which represents the amount of variance of the p.d.f. of the small-scale signal generated in the conversion from time series into space series, as obtained from (9.6) (see § 9).

effects are linear for fluctuations of the large-scale signal close to zero. Nevertheless, the interaction between the large- and small-scale motions is generally nonlinear, especially for $u^*_L < 0$. We can also observe that the trend does not change with the radial location of the jet. This is consistent with Bandyopadhyay & Hussain (1984), where the correlation coefficients between the large-scale signal and the envelope of the small-scale signal are observed to remain constant across different radial positions.

Moreover, the correlation coefficient (R) between the large-scale signal and the envelope of the small-scale signal allowed further evaluation of the interaction between the scales. The envelope of the small-scale signal is calculated following the approach by Mathis *et al.* (2009). The Hilbert transform was first applied to the small-scale signal. For the envelope, we filtered the Hilbert-transformed signal using the same spectral filter as for the large-scale fluctuations. To estimate a possible time delay in the interaction between the scales, we calculated the correlation coefficient R for different time shifts Δt of the two signals. As a convention, a negative time shift is equivalent to delaying the small-scale signal. Figure 5 shows the result of this procedure. The maximum correlation coefficient ($R = 0.65$) is found for a negative shift of 1.8×10^{-4} s, implying a delay in the scale interaction. This shift is almost equal to the Kolmogorov time scale $\tau_\eta = 2 \times 10^{-4}$ s. The interaction between large and small scales can therefore be considered concurrent.

A test was performed to check the sensitivity of small-scale amplitude modulation to the choice of the large-scale frequency content. In this test, the large-scale signal was associated with the ranges $\lambda_T - L$, and $3\lambda_T - L$, in which the lower limit of the range was varied with respect to the definition of large-scale motions introduced in § 3, $2\lambda_T - L$. The small-scale signal was kept the same as before. With these new large-scale bounds, the analysis presented in this section was repeated, and the results showed that changes in the strength of the physical phenomenon are negligible.

https://doi.org/10.1017/jfm.2015.227 Published online by Cambridge University Press

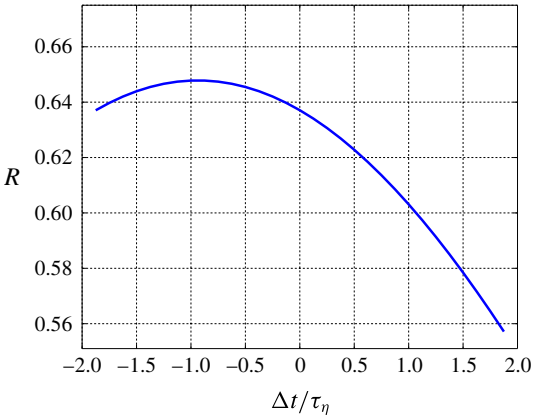

FIGURE 5. (Colour online) Correlation coefficients R for different relative time shifts between the large-scale signal and the envelope of the small-scale signal (following Mathis *et al.* 2009).

5. Frequency modulation

In this section the frequency modulation of the small-scale motions is examined. We apply the peak and valley counting (PVC) method (Ganapathisubramani *et al.* 2012) to the present dataset of HWA, with the aim of quantifying the extent of frequency modulation with the strength of large-scale fluctuation. This approach is based on the counting of the local number of peaks and valleys (hence its name) in the small-scale signal over a certain time segment. The metric was developed with the aim of overcoming the limitations linked with the zero-crossing method. A u_L^* binning with a spacing of 0.05 ranging from $u_L^* = -0.4$ to $u_L^* = 0.4$ was created for the large-scale fluctuations, similar to what was done in § 4. Moreover, the time series of both the large- and small-scale fluctuations were divided into segments of 100 samples each (corresponding to 5×10^{-4} s). This segment size was chosen as the ratio between the acquisition frequency and 2001 Hz, a frequency intermediate between the large- and small-scale motions. With such a bin size and time segment, the minimum amount of samples falling within each bin was 400. The number of local maxima and minima of the small-scale signal within each time segment was then determined. A representative frequency of occurrence of local maxima and minima per unit length $\langle f_m \rangle$ was obtained by dividing the number of local maxima and minima by 10^{-3} s, i.e. twice the length of the time segment. Eventually, the number of local maxima and minima was conditionally averaged depending on the local strength of the large-scale fluctuation u_L^*. In figure 6, the result of the application of the PVC scheme to the hot-wire dataset is presented, for the signals acquired at the centreline and at 0.2 non-dimensional radii. The two graphs show a similar trend for both the radial positions within the jet. It can be seen that the frequency of the small-scale signal increases statistically with the strength of the large-scale fluctuations. As for the amplitude modulation, the relation is generally nonlinear.

However, the frequency modulation can also be regarded as a frequency dependence in the amplitude modulation, that is, different frequencies experience a different level of amplitude modulation (for a given u_L^*). It thus appears that the higher frequencies of the small-scale signal are more amplitude-modulated. If we look at this in the frequency domain, we can expect that the higher wavenumbers within the viscous

https://doi.org/10.1017/jfm.2015.227 Published online by Cambridge University Press

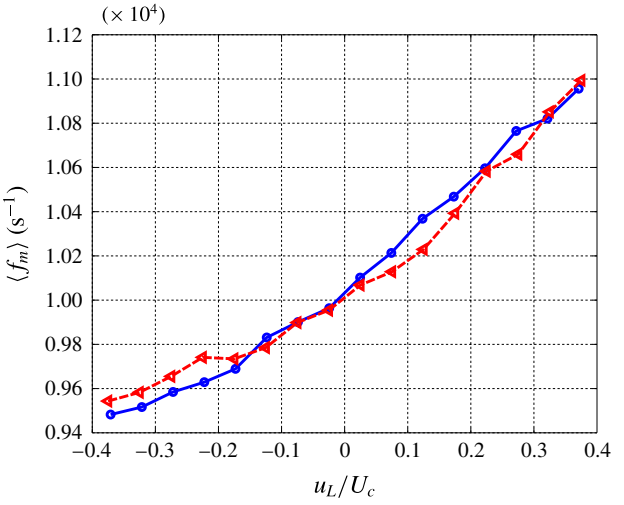

FIGURE 6. (Colour online) Local frequency of the small-scale signal $\langle f_m \rangle$, conditioned on the fluctuations of the large-scale signal, for a signal acquired at the centreline position (continuous line, ○), and at 0.2 non-dimensional radii (dashed line, ◁), both at $x/D = 70$.

region are subject to stronger amplitude modulation. This would have an important implication. The behaviour of the large scales alters the shape of the velocity power spectrum locally. In particular, the small-scale frequency band is expected to become flatter for positive fluctuations of the large-scale signal, and steeper for negative fluctuations. In order to verify this, the following procedure was implemented.

(i) First, the small-scale signal was divided into segments of length corresponding to 200 time samples (10^{-3} s).
(ii) A hamming filter was applied to the segments of the small-scale signal.
(iii) From all the filtered segments, we selected only those with a particular value of u_L^* in the corresponding large-scale signal.
(iv) The selected pieces of the small-scale signal were juxtaposed, thus generating new signals.
(v) The power spectra for each of these conditional signals were calculated. Finally, the obtained conditional power spectrum was normalized by its value at $k\eta = 10^{-0.6}$, to compensate for the differences in the energy content and emphasize the slope of the spectrum.

This scheme was applied for three different u_L^*. The results are shown in figure 7. The power spectrum was first conditioned on strong large-scale fluctuations u_L^* ranging between 0.3 and 0.35 (positive fluctuations), then between -0.35 and -0.3 (negative fluctuations), and eventually for randomly selected segments of the small-scale signal (unconditional u_L^*). As predicted, the slope of the line indicating strong negative fluctuation is the steepest, whereas the slope for strong positive fluctuation is flatter. This supports the earlier statement that the amplitude modulation of the small-scale signal is frequency-dependent, and that the degree of amplitude modulation increases at higher frequencies. Consistent with this finding, Fiscaletti *et al.* (2013) obtained that small-scale signals associated with higher frequencies present a higher amplitude modulation when quantified as in § 4.

https://doi.org/10.1017/jfm.2015.227 Published online by Cambridge University Press

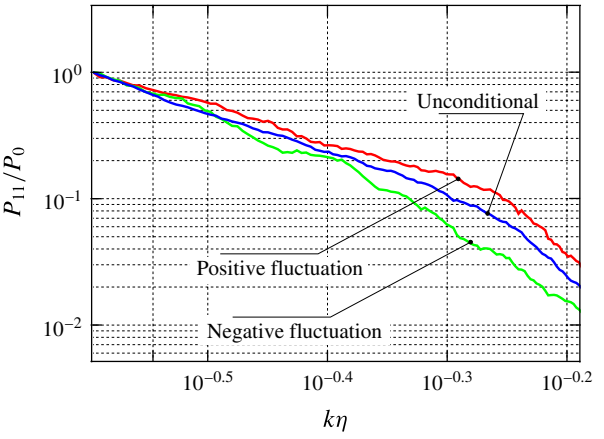

FIGURE 7. (Colour online) Power spectra of conditionally selected segments of the small-scale signal. The positive fluctuation line is obtained for u_L^* ranging between 0.3 and 0.35, the negative fluctuation line is between -0.35 and -0.3, and the line labelled 'Unconditional' is obtained for unconditional u_L^* (randomly selected segments of the small-scale signal).

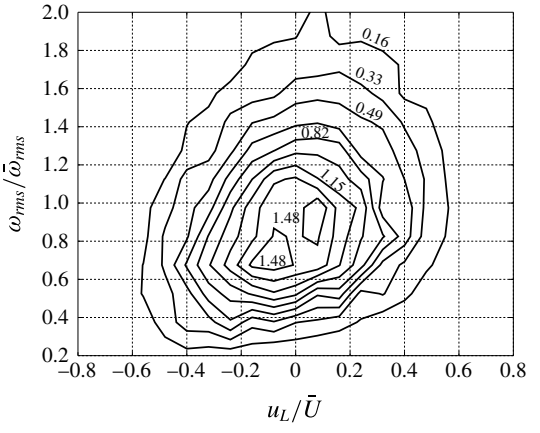

FIGURE 8. Joint probability density function between the r.m.s. vorticity over each field of view ω_{rms} and the average axial velocity over each field of view. The vorticity was normalized over the total r.m.s. vorticity, and the average axial velocity over the average axial velocity of the flow.

6. The coupling between small-scale flow structures and large-scale fluctuations

The observed small-scale amplitude modulation leads us to hypothesize that vorticity and dissipation, which are closely associated with small scales, are on average more intense in regions of positive large-scale fluctuations. In order to check this assumption, the joint probability density functions (j.p.d.f.s) between the r.m.s. vorticity and dissipation and the large-scale velocity fluctuations u_L^* were calculated from the PIV velocity fields. Note that the large-scale velocity fluctuation was taken as the average axial velocity fluctuation over the field of view, as explained in § 3. The number of samples considered was 11 000, namely the total number of velocity fields acquired from μPIV. The results are shown in figures 8 and 9. At negative

https://doi.org/10.1017/jfm.2015.227 Published online by Cambridge University Press

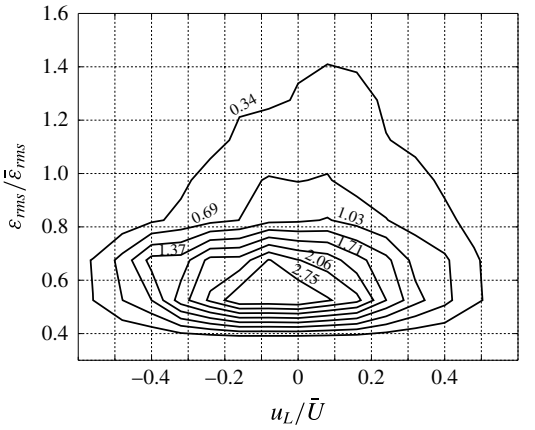

FIGURE 9. Joint probability density function between the r.m.s. rate of dissipation over each field of view ε_{rms} and the average axial velocity over each field of view. The rate of dissipation was normalized over the total r.m.s. rate of dissipation, and the average axial velocity over the average axial velocity of the flow.

large-scale fluctuations, the vorticity r.m.s. is mostly lower than the average r.m.s. of the vorticity magnitude, computed over all the samples. A similar trend can be observed for the dissipation r.m.s. Moreover, as the large-scale fluctuations increase, vorticity and dissipation r.m.s. tend to increase too. Therefore, regions of the flow that have a large-scale axial velocity higher than the average axial velocity of the flow are characterized by higher levels of vorticity and dissipation, and *vice versa*.

This finding is consistent with amplitude modulation observed in § 4 based on the HWA data. Furthermore, we estimated the amplitude modulation from the long-range μPIV dataset for comparison with HWA. We applied a procedure similar to that used in § 4, for the HWA dataset. The procedure consists of the following steps.

(i) The axial small-scale velocity r.m.s. and the vorticity r.m.s. of each of the 11 000 vector fields was calculated, relative to the average axial velocity and vorticity computed over the vector field, respectively.
(ii) Equally spaced bins with a spacing of 0.125 ranging from $u_L^* = -0.375$ to $u_L^* = 0.375$ were created.
(iii) Depending on the value of the u_L^*, the associated axial velocity r.m.s. and vorticity r.m.s. was included in a group, corresponding to one of the u_L^* bins.
(iv) The average axial velocity r.m.s. and vorticity r.m.s. included in each u_L^* bin were computed.

The results of these calculations are given in figure 10. A first consideration that can be retrieved from these graphs is that the axial velocity r.m.s. and the vorticity r.m.s. provide almost the same results when it comes to the quantification of the amplitude modulation. Amplitude modulation from PIV shows a trend similar to the HWA analysis. However, the nonlinearity observed for strongly negative large-scale fluctuations in the analysis of HWA time series (figure 4) cannot be found in PIV (figure 10). Moreover, we can see that the level of amplitude modulation for long-range μPIV is much lower than for HWA (i.e. the slope of the graph is smaller). In particular, we can notice that the amplitude modulation for strongly positive fluctuations ($u_L^* > 0.3$) and strongly negative fluctuations ($u_L^* < -0.3$) is around 10 %

https://doi.org/10.1017/jfm.2015.227 Published online by Cambridge University Press

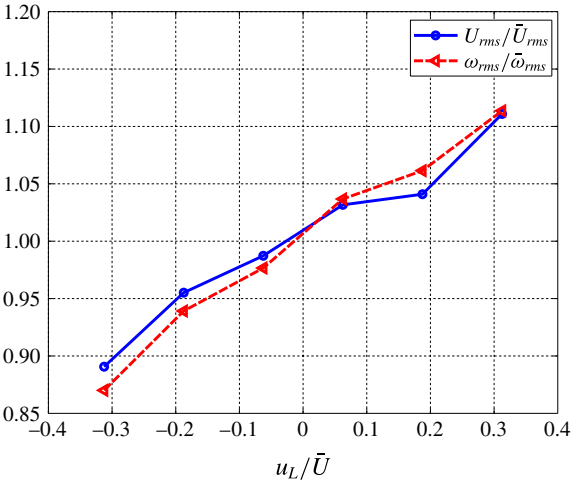

FIGURE 10. (Colour online) Average axial velocity r.m.s. (continuous line, ○) and average vorticity r.m.s. (dashed line, ◁) computed over each vector field, conditioned on the fluctuations of the large-scale signal u_L, from the long-range μPIV dataset.

of the unconditional r.m.s. (figure 10), whereas it reaches values up to 35 %–40 % if we look at the dataset from HWA (figure 4). This overestimation of the amplitude modulation from HWA can be attributed to the Taylor hypothesis of frozen turbulence in the conversion from time to space series of HWA, which is discussed in § 9.

7. The conditional size of the vorticity structures

Next, we examine the size of the coherent structures of vorticity depending on the large-scale flow velocity. This is of interest since changes in structure size could potentially be linked to frequency modulation observed in the previous sections. An indication of the diameter of the vortices (called 'worms') can be found in the literature for flows at different Re_λ. In this respect, Jiménez *et al.* (1993) showed that the core diameter of these intense vortices scales with the Kolmogorov length scale. This inference was obtained from DNS simulations of isotropic turbulence run at different Reynolds numbers. Nevertheless, the Taylor microscale Reynolds number (Re_λ) of these simulations was never higher than 150 ($Re_\lambda < 150$). Kaneda & Ishihara (2006) have recently examined the size of the intense vortices in a DNS of homogeneous isotropic turbulence at a Taylor microscale Reynolds number higher than 1000 ($Re_\lambda > 1000$). Ganapathisubramani *et al.* (2008) confirmed from experiments the characteristic size and spatial organization of the structures of intense vorticity previously observed; subsequently, Fiscaletti *et al.* (2014) were able to investigate experimentally the scaling of the worms at a Taylor microscale Reynolds number (Re_λ) of around 350. In all the aforementioned works, the characteristic core diameter of the structures of intense vorticity was found to range between 8η and 12η. In the present work, the size of the coherent structures of vorticity is analysed conditioned on positive and negative large-scale fluctuations. Recall that the average of the axial velocity over the field of view was regarded as the large-scale fluctuation in the μPIV measurement. An estimate of the average size of the intense vortices can be obtained from the autocorrelation coefficient map of the out-of-plane

https://doi.org/10.1017/jfm.2015.227 Published online by Cambridge University Press

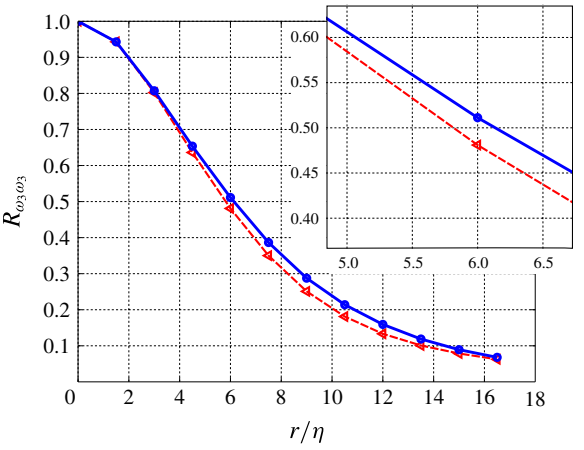

FIGURE 11. (Colour online) Autocorrelation coefficient maps of the out-of-plane vorticity for in-plane shifts r, conditioned on the large-scale signal $u_L^* > 0.3$ (dashed line, ◁) and $u_L^* < -0.3$ (continuous line, ○). The local fluctuation of the large-scale signal is defined in § 3; μPIV data have been analysed here.

vorticity ω_3. In figure 11, the cross-sections of the autocorrelation peak are given conditioned on $u_L^* < -0.3$ and $u_L^* > 0.3$. The number of samples that contributed to the autocorrelation map were 1415 for $u_L^* > 0.3$, and 1408 for $u_L^* < -0.3$. As a threshold for the identification of the characteristic core radius, we considered an autocorrelation coefficient of 0.5 (figure 11). It can be inferred that the characteristic diameter of the structures of intense vorticity is larger ($\approx 12.2\eta$) if conditioned on $u_L^* < -0.3$, and smaller ($\approx 11.8\eta$) if conditioned on $u_L^* > 0.3$ of around 3.3 % depending on u_L^*. Furthermore, we analysed the spatial extent of the 500 most intense vortices, detected for large-scale fluctuations $u_L^* > 0.3$ as well as the 500 most intense vortices within $u_L^* < -0.3$ regions. The intensity of each vortex was evaluated as the maximum value of λ_{ci} among the points making up each vortex. With the aim of quantifying the extension of the 500 vortices, the point characterized by the highest λ_{ci} was surrounded by a square box of $15\eta \times 15\eta$ in size (so as to include the entire core diameter of the vortex, expected to be around 10–12η, as mentioned above). The number of points of the box complying with

$$\lambda_{ci} > C_e\, \lambda_{ci,max} \tag{7.1}$$

were considered as part of the vortex, and represented an estimate of the characteristic area of each vortex. The result depends on the chosen value of the C_e parameter. The procedure was developed for its intrinsic robustness, and yielded the graph in figure 12, showing the square root of the average intense vortex area conditioned on $u_L^* < -0.3$ and $u_L^* > -0.3$ for different C_e. The square root of the area in this case is again a measure for the characteristic vortex diameter. It can be seen that the intense vortices located in regions of strongly positive fluctuations are smaller than the intense vortices located in regions of strongly negative fluctuations. These observations are consistent with the analysis of the ω_3 autocorrelation peaks discussed above.

Moreover, we estimated the size of a 'local' Kolmogorov length scale for positive and negative fluctuations of the large-scale signal from the dataset of HWA. The rate of dissipation conditioned on the strength of the large-scale fluctuations was therefore

https://doi.org/10.1017/jfm.2015.227 Published online by Cambridge University Press

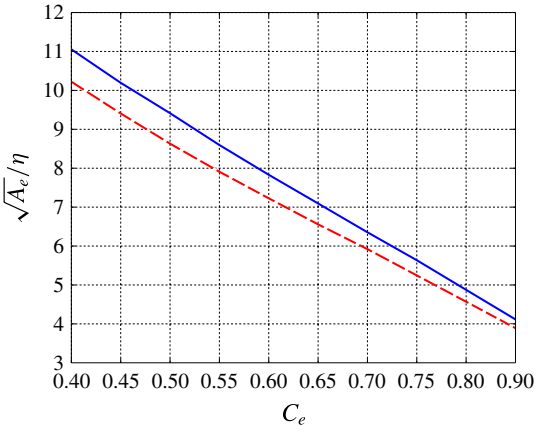

FIGURE 12. (Colour online) Characteristic size of the 500 most intense vortices for different values of the threshold C_e (7.1), conditioned on $u_L^* > 0.3$ (dashed line) and $u_L^* < -0.3$ (continuous line).

computed. In particular, the Kolmogorov length scale was estimated for $u_L^* > 0.3$ (strongly positive fluctuations) and for $u_L^* < -0.3$ (strongly negative fluctuations). On the unfiltered velocity fluctuations, we applied the following central difference scheme, which relies on the hypothesis of isotropy, already generally ascertained in Fiscaletti *et al.* (2014) for the experimental object of the present analysis:

$$\varepsilon = \left\langle 15\nu \left[(u(i+1) - u(i-1)) \Big/ 2 \left(\frac{\bar{U} + u(i)}{f} \right) \right]^2 \right\rangle, \tag{7.2}$$

where f is the acquisition frequency. From this, we retrieved the rate of dissipation conditioned on the positive (ε^+) and negative (ε^-) fluctuations of the large-scale signal. The conditional Kolmogorov length scale could then be computed, yielding

$$\eta^+ = \left(\frac{\nu^3}{\varepsilon^+} \right)^{(1/4)} = 56.0 \ \mu\text{m}, \tag{7.3}$$

$$\eta^- = \left(\frac{\nu^3}{\varepsilon^-} \right)^{(1/4)} = 57.3 \ \mu\text{m}, \tag{7.4}$$

obtained for $\varepsilon^+ = 366.4 \ \text{m}^2 \ \text{s}^{-3}$ and $\varepsilon^- = 333.8 \ \text{m}^2 \ \text{s}^{-3}$. Therefore the positive large-scale fluctuations are associated with a stronger rate of dissipation locally and a smaller size of the local Kolmogorov length scale. The percentage difference in the two estimated Kolmogorov length scales is 2.3 %. This is in good agreement with the percentage difference found earlier for the characteristic diameter of the vortices, which are known to scale on η.

To summarize, an increase in the strength of the large-scale fluctuations ($u_L^* \uparrow$) is associated with a decrease in the size of the local Kolmogorov length scale ($\eta \downarrow$). This change was estimated to be in the order of 2 %–3 % if we move from strongly positive fluctuations ($u_L^* > 0.3$) to strongly negative fluctuations ($u_L^* < -0.3$). In relation to the observed magnitude of the amplitude and frequency modulation, these size effects can thus be considered negligible.

https://doi.org/10.1017/jfm.2015.227 Published online by Cambridge University Press

K	$\bar{V}$ (m s^{-1})	N
2.0	10.26	38 889
3.0	10.37	16 662
4.0	10.42	7 747
5.0	10.47	3 847
6.0	10.48	2 011
7.0	10.50	1 071

TABLE 2. Average convection velocities of the vortices $\bar{V}$ (second column) after applying different thresholds K for λ_{ci} (3.1). N represents the total number of vortices found for the given value of K. Note that the average convection velocities of the vortices are higher than the average axial velocity of the flow, at $\bar{U} = 9.78$ m s^{-1}.

8. The conditional intensity of the coherent structures

In the previous section we showed that the size of the coherent structures of vorticity does not change significantly with u_L^*. If the structure size is unaffected, the observed amplitude modulation must then be explained by the spatial distribution of the intense coherent structures relative to the large-scale motions, which will be examined next. The criterion for the detection of the intense vortices and the identification of their centres is detailed in § 3. We assigned different values to the threshold parameter K in (3.1), thus detecting a decreasing number of vortices with increasing values of K. The vortex convection velocity (V) was then taken as the measured flow velocity at the centre. A summary of the total number of vortices and their average convection velocity for a given threshold K is provided in table 2. The average velocity at which the intense vortices are convected downstream is always higher than the mean axial component of the velocity ($\bar{U} = 9.78$ m s^{-1}). In particular, the vortices characterized by higher λ_{ci} tend to be convected at higher velocities. Further evidence of this trend can be found in the j.p.d.f. between the convection velocity of the vortices and their intensity, taken as the peak λ_{ci} of the vortex. The j.p.d.f. was computed for $K = 3$, thus examining a total number of 16 662 vortices (second row of table 2). The resulting j.p.d.f. is shown in figure 13. It can be observed that the most intense vortices are characterized by higher convection velocities, which means that they are found more often in high-velocity regions of the flow, as compared to regions characterized by low velocity.

As already ascertained in other works (i.e. Ganapathisubramani *et al.* 2008; Fiscaletti *et al.* 2014), the regions of intense dissipation appear in the vicinity of intense vortices. A similar trend to that observed for the average absolute vorticity could therefore also be expected for the structures of intense dissipation rate. In order to identify the regions of intense dissipation we used (3.3) for different values of the parameter K_ε. The flow velocity at the centroids of each region of intense dissipation was evaluated and taken as the convection velocity. In table 3 we give a summary of the whole number of regions of intense dissipation, and the average convection velocity (V_ε) for a given threshold K_ε. Similar to the vortices, the structures of intense dissipation are convected downstream at a velocity higher than the average flow velocity, and increasing with the strength K_ε. We compute the j.p.d.f. between the convection velocities of the regions of intense dissipation and their dissipation rate. Equation (3.3) was used to identify the regions of intense dissipation, with $K_\varepsilon = 3$ as value of the K_ε parameter. The j.p.d.f. is given in figure 14. As for the

https://doi.org/10.1017/jfm.2015.227 Published online by Cambridge University Press

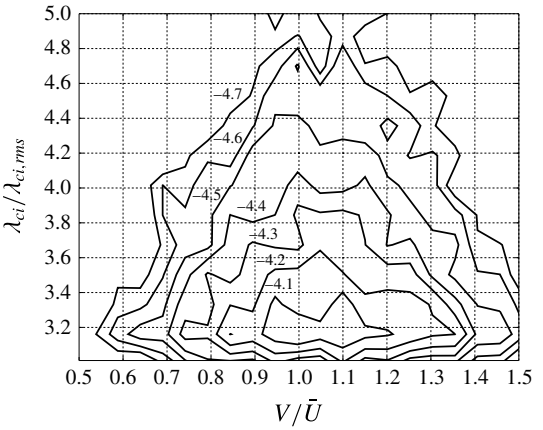

FIGURE 13. Joint probability density function between the strength of the intense vortices λ_{ci} and their axial convection velocity V. The intense vortices were detected with the λ_{ci}-criterion (after Zhou *et al.* 1999, (3.1)), with $K = 3$. The j.p.d.f. is based on 16 662 samples (second row of table 2).

K_ε	$\bar{V}_\varepsilon$ (m s^{-1})	N
2.0	10.35	31 780
3.0	10.45	17 057
4.0	10.53	9 966
5.0	10.57	6 208
6.0	10.58	4 122
7.0	10.58	2 802

TABLE 3. Average convection velocities of the regions of intense dissipation $\bar{V}_\varepsilon$ (second column) after applying different thresholds K_ε for ε (3.3). N represents the total number of regions of intense dissipation found for the given value of K_ε. Note that the average convection velocities of the regions of intense dissipation are higher than the average axial velocity of the flow, at $\bar{U} = 9.78$ m s^{-1}.

structures of vorticity, the structures of intense dissipation characterized by higher intensity are typically convected downstream at higher velocities.

To summarize, more intense small-scale structures (i.e. vortices and dissipation structures) are typically located within regions of high flow velocity, so they are expected to be convected at higher velocity. This finding can be related to the evidence of amplitude and frequency modulation described in previous sections. In particular, the positive correlation between the intensity of a vortex and its convection velocity can be directly related to the trend between the strength of the large-scale fluctuation and the local standard deviation of the small-scale signal (figure 4).

9. The effects of the Taylor hypothesis of frozen turbulence

We now move to the evidence of frequency modulation that was ascertained in § 5. In that section the local strength of the large-scale fluctuations was found to modulate the number of peaks and valleys of the small-scale signal locally (figure 6). This was regarded as evidence of frequency modulation, with the amplitude modulation being

https://doi.org/10.1017/jfm.2015.227 Published online by Cambridge University Press

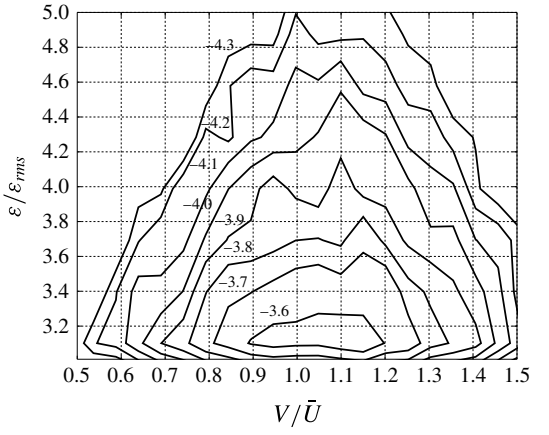

FIGURE 14. Joint probability density function between the rate of dissipation of the regions of intense dissipation ε and their axial convection velocity V_ε. The regions of intense dissipation were detected with the criterion detailed in § 3 (3.3), with $K_\varepsilon = 3$. The j.p.d.f. is based on 17 057 samples (second row of table 3).

frequency-dependent. Moreover, a frequency dependence in the already ascertained amplitude modulation implies a local change of the slope of the power spectrum conditioned on the local strength of the large-scale fluctuation. In this respect, the two conditional spectra in figure 7 were interpreted as evidence of frequency modulation. However, if we admit that the small-scale structures do not change in size, as ascertained in § 7, the frequency modulation is then a direct consequence of the different convection velocities at which the intense vortices are convected downstream. In particular, the small-scale fluctuations residing in a positive large-scale fluctuation ($u_L^* > 0$) will probably be convected past the hot-wire probe faster (than the average flow velocity), resulting in an increased number of peaks and valleys per unit time ($V \uparrow$ implies $P\&V \uparrow$) relative to the same-sized small-scale features in a negative u_L^* associated with lower convection velocity. If we analyse more carefully the two conditional power spectra (figure 7), we can see that they collapse onto each other for the first part of the viscous region (for $k\eta$ ranging between $10^{-0.6}$ and $10^{-0.42}$). Furthermore, the spectra without rescaling the vertical axis (figure 15*a*) seem to have the same shape in the region $10^{-0.6}$–$10^{-0.42}$, and thus mainly reveal an offset. Nevertheless, it is possible to compensate to first order for the non-constant convection velocity in the conditional spectra, using

$$\frac{\Delta k}{k_T} = \frac{u_L}{U_c} - 1, \tag{9.1}$$

where Δk is the wavenumber shift of the conditional spectrum relative to the Taylor hypothesis (which is to be compensated), k_T is the wavenumber after application of the Taylor hypothesis at constant convection velocity by the mean flow U_c, i.e. the average axial velocity of the flow ($U_c = 10.56$ m s^{-1}); the large-scale velocity fluctuation u_L is then taken as the difference between the real convection velocity of the conditional small scales and U_c. For the present conditional spectra, $u_L = 0.3U_c$ for the positive large-scale fluctuations, and $u_L = -0.3U_c$ for the negative. The result of this compensating shift is given in figure 15(*b*). The two conditional spectra

https://doi.org/10.1017/jfm.2015.227 Published online by Cambridge University Press

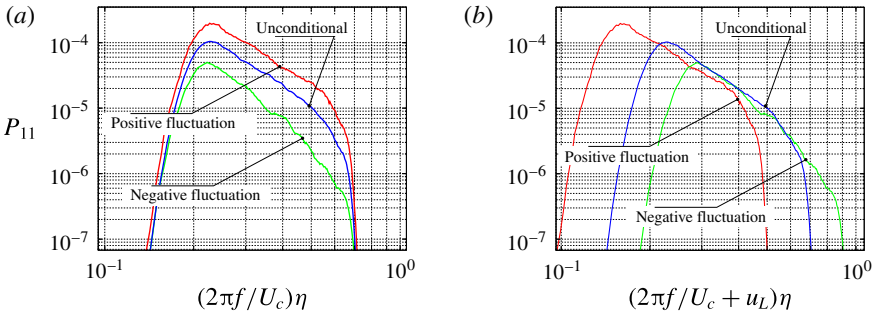

FIGURE 15. (Colour online) Power spectra of conditionally selected segments of the small-scale signal, (*a*) before and (*b*) after the compensation for the horizontal offset induced by the Taylor hypothesis of frozen turbulence in the conversion of time series into space series. The positive fluctuation line is obtained for u_L^* ranging between 0.3 and 0.35, the negative fluctuation line is between -0.35 and -0.3, and the line labelled 'Unconditional' is obtained for unconditional u_L^* (randomly selected segments of the small-scale signal).

(figure 15*b*) now overlap on the unconditional one, thus strongly suggesting that the three power spectra are actually different portions of the same spatial power spectrum. Moreover, the collapse of the conditional spectra (figure 15*b*) supports that the modulation in frequency of the small scales can largely be explained as an effect induced by variations in the convection velocity of the same small (spatial) scales.

The application of the Taylor hypothesis in the conversion of time series into space series also affects the estimate of the amplitude modulation from HWA data (figure 4). The adoption of the same band-pass frequencies independently of the local convection velocity leads to a different spatial frequency content in the various segments of the small-scale signal, depending on the strength and the sign of the associated large-scale fluctuations. As a consequence, the power spectrum conditioned on strongly positive fluctuations includes energy contributions from lower spatial frequencies than those corresponding to the prescribed range of 1.5–5η (§ 3), whereas the power spectrum conditioned on strongly negative fluctuations includes contributions from higher spatial frequencies than those corresponding to the prescribed range 1.5–5η (figure 15*b*). Because of the slope in the power spectrum, this produces a larger energy content in the power spectrum conditioned on strongly positive fluctuations, and *vice versa*. Therefore, all the segments of the small-scale signal associated with positive large-scale fluctuations contain an increment of energy produced by the Taylor hypothesis. This energy increment can be estimated by comparing the amplitude modulation from HWA (figure 4) and from long-range μPIV (figure 10). In fact, data from long-range μPIV are not affected by such a frequency shift (because the spatial frequencies are measured directly), so they can thus be considered representative of the real amplitude modulation in space. For turbulent jet flow, we can assess that around 75 % of the amplitude modulation estimated from HWA comes from the conversion from time series into space series, namely by application of the Taylor hypothesis of frozen turbulence.

An estimate of the amount of amplitude modulation in consequence of the conversion from time series into space series can also be obtained analytically. Consider the turbulent kinetic energy of the signal at a certain wave number $\widehat{E}(k)$, which can be modelled by a power law in the small-scale range:

$$\widehat{E}(k) = C\,k^{-p} = \tfrac{1}{2}u_k^2, \tag{9.2}$$

https://doi.org/10.1017/jfm.2015.227 Published online by Cambridge University Press

where, from experimental data, p is approximately 2 in the range of $k\eta$ between 1.5 and 5, C is a constant independent of k, and u_k is the velocity fluctuation associated with k. Equation (9.2) can be rewritten as

$$|u_k| = \widehat{C}\, k^{-(p/2)}, \tag{9.3}$$

where $\widehat{C} = \sqrt{2C}$. The wavenumber $\bar{k}$ (in space) can be replaced by the ratio between the frequency (f_k) and the local convection velocity. The local convection velocity can be approximated as the sum between the mean velocity of the flow, and local large-scale velocity fluctuation ($U_{CV} = U_c + u_L$). The smaller scales contain much less and can therefore be neglected. We obtain

$$\bar{k} = \frac{f_k}{U_c + u_L} \tag{9.4}$$

which, if plugged into (9.3), yields

$$|u_k| = \widehat{C}\left(\frac{f_k}{U_c + u_L}\right)^{-(p/2)}. \tag{9.5}$$

If this expression for u_k is expanded in Taylor series, we can estimate the local amplitude of the small-scale signal in relation to the strength and the sign of the large-scale fluctuation (u_L):

$$\begin{aligned} |u_k| &= |u_k|\Big|_{(u_L=0)} + \frac{\partial |u_k|}{\partial u_L}\Big|_{(u_L=0)} u_L + \text{h.o.t.} \\ &\approx \left(\frac{f_k}{U_c}\right)^{-(p/2)} \left(1 + \frac{p}{2}\frac{u_L}{U_c}\right). \end{aligned} \tag{9.6}$$

If now in a HWA measurement the small scales are defined by a constant temporal frequency f_k, then it can be seen from this equation that the observed amplitude of the small-scale signal increases/decreases linearly with the strength of the positive/negative large-scale fluctuations. This linear trend is added to figure 4 (dotted line, $*$). If we consider a large-scale fluctuation of $u_L/U_c = 0.3$ and $p = 2$, we obtain that the amount of amplitude modulation generated in the conversion of the time series into space series is 0.3. The amplitude modulation obtained from the analysis described in § 4 is 0.42 for the signal at the centreline. This means that the amount of amplitude modulation introduced in the conversion of the hot-wire signal from time series into space series accounts for around 70 % of the total amplitude modulation. This analytical result compares well with the observed difference in modulation from HWA and PIV (§ 4).

Overall, this overestimation can also be interpreted as the difference between the scale interactions in space and time. Based on the comparison, it can be seen that the interactions in time (i.e. in hot-wire data) appears to be more 'active' than interactions in space. This suggests that flow evolution in time is perhaps more important to scale interactions compared to the concurrent spatial structure.

https://doi.org/10.1017/jfm.2015.227 Published online by Cambridge University Press

10. Analysis of a turbulent boundary layer

We now explore how the present findings for jet flow may apply to TBL flow. From the analysis of jet flow we learned that the observed amplitude modulation in a jet can be viewed as a spatial (inhomogeneous) organization of the small scales. In particular, the small-scale vortices are more often located in high-velocity regions as opposed to the low-speed regions within the jet. If we assume that in a TBL the size of the small-scale features does not change significantly, as in the jet, or if we simply consider a specific physical length scale within the small-scale range, we can relate this spatial organization to amplitude and frequency modulation in frequency space (HWA), as mentioned. Regarding the spatial organization of the small scales or alternatively the vortex structures, the experimental studies by Adrian, Meinhart & Tomkins (2000) and Elsinga *et al.* (2010), and the DNS simulations by del Álamo & Jiménez (2009) are examined here.

In figure 21 of the work by Adrian *et al.* (2000), the conditionally averaged streamwise convection velocities of the coherent structures of vorticity are presented at different wall distances. It can be observed that for small distances from the wall, the streamwise convection velocities are almost equal to the average streamwise velocity of the flow. However, if we move to the outer region, the streamwise convection velocities are lower than the average streamwise velocity of the flow. In their investigation, the Reynolds number of the flow is $Re_\theta = 7705$, corresponding to a Reynolds number based on the Taylor microscale higher than 350. Subsequently, the DNS simulations by del Álamo & Jiménez (2009) and the experiments by Elsinga *et al.* (2010) confirmed this trend. In the outer region of a TBL, the convection velocities of the coherent structures of vorticity are lower than the local average velocity of the flow, which explains the stronger activity of the small scales for negative fluctuations of the large-scale signal, as found from HWA data. Furthermore, figure 2(*a*) of del Álamo & Jiménez (2009) shows the streamwise convection velocities of the small scales (i.e. small wave length), in a channel flow. The bottom graph reveals that at 10 wall units distance from the wall the convection velocities are higher than the local average streamwise velocities of the flow. This implies that, in the near-wall region of the boundary layer, the small-scale structures are typically located in large-scale high-speed regions, thus producing the positive amplitude modulation effects already ascertained in the aforementioned studies.

Moreover, the observations of §§ 6 and 9 have shown that the effects produced by variations in convection velocity are embedded in the amplitude modulation measured with HWA. These effects led us to estimate the amplitude modulation to be four times higher when based on time series (HWA) as opposed to that returned in space by PIV. We showed that, in the viscous region of the spectrum, all the spectra conditioned on the strength of the large-scale fluctuation collapse approximately on the same spectrum when a compensating horizontal shift is introduced (figure 15). From the experimental dataset described in the work by Ganapathisubramani *et al.* (2012), we intend to verify if an analogous collapse in the conditional spectra can be found in the near-wall region of a TBL. Figure 16(*a*) provides the result of this analysis. As can be observed, the three spectra conditioned on strongly positive, zero, and strongly negative fluctuations of the large-scale signal show a collapse for an interval of non-dimensional frequencies $\left((2\pi f/U)\delta\right)$ between 4×10^2 and 3×10^3. This frequency range represents only a small and low energetic portion of the whole interval of frequencies representative of the small-scale motions, as defined in the work by Ganapathisubramani *et al.* (2012). This implies that only the frequency modulation can be explained as the result of the Taylor hypothesis.

https://doi.org/10.1017/jfm.2015.227 Published online by Cambridge University Press

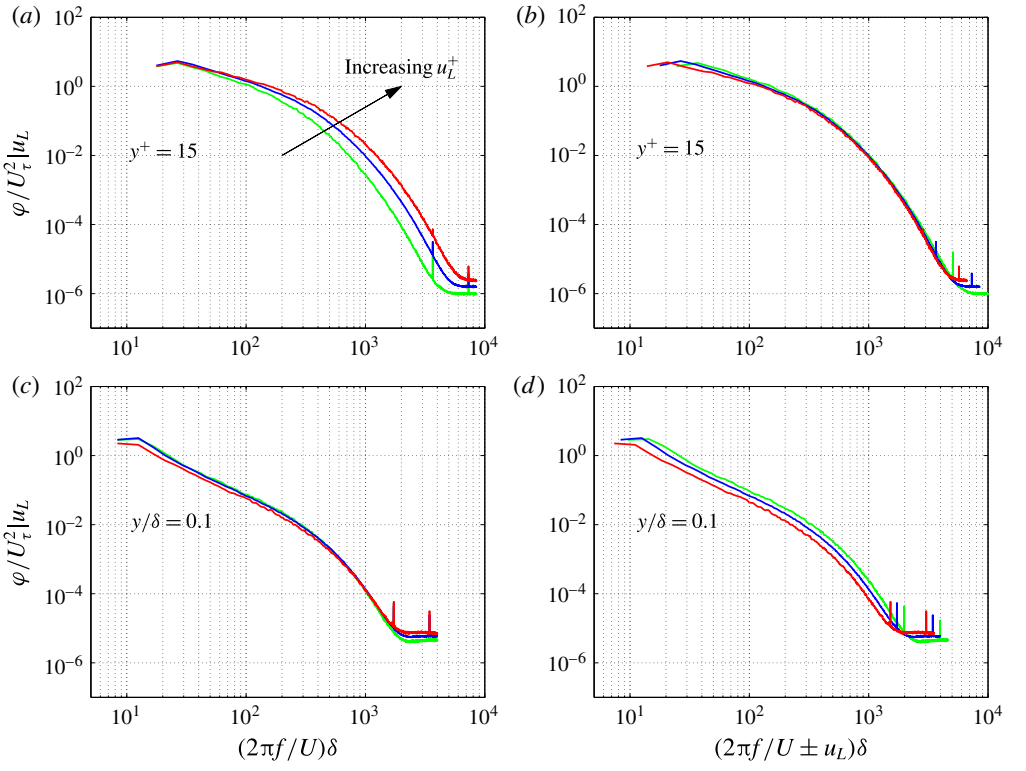

FIGURE 16. (Colour online) Conditional power spectra of the small scales as a function of wavenumber at (*a,b*) $y^+ = 15$ and (*c,d*) $y/\delta = 0.1$. The horizontal axis shows the wavenumber computed with free-stream velocity (*a,c*) and with an appropriate local convection velocity (*b,d*). The different lines show the conditional spectra of the small scales for $u_L^* = -3$, 0 and 3. Note the collapse of the spectra at higher frequencies at $y^+ = 15$ and increased deviation at $y/\delta = 0.1$ when the correction for local convection velocity is employed. Figure adapted from Ganapathisubramani *et al.* (2012).

Frequency modulation has been determined by means of the peak and valley counting method (PVC), and the number of local maxima and minima is mainly determined by the high-frequency components of the signal. Therefore the collapse of the three spectra at the high frequencies shows that the frequency modulation is actually the result of different convection velocities of the structures of vorticity, analogous to the jet. It is instead more difficult to draw conclusions for amplitude modulation. Many factors cause the analysis in the near-wall region of a TBL to be different from that in jet flow: (i) the important phase delay in the top-down interaction between scales, as shown by Ganapathisubramani *et al.* (2012) (their figure 11*a*), (ii) the different definition of the small-scale motions between the present investigation ($<5\eta$) and the works from the literature on TBLs (typically $<\delta$), (iii) the modest slope of the power spectrum in the near-wall region, for the most energetic frequencies.

It is also of interest to move to the outer region of a TBL and perform the same analysis. The outer region is characterized by a negative correlation coefficient between the large-scale and small-scale signals. In this region of the flow we expect that the spectrum conditioned on positive large-scale fluctuations has a lower energy content than the spectrum conditioned on negative large-scale fluctuations,

https://doi.org/10.1017/jfm.2015.227 Published online by Cambridge University Press

as a consequence of amplitude modulation. Analogously to the near-wall region, the three conditional spectra from Ganapathisubramani *et al.* (2012) are given in figure 16(*c,d*). It can be observed that the difference in the energy content of the three spectra is small, even without any horizontal compensating shift. This is probably due to the simultaneous effects of both the local convection velocities and the amplitude modulation, which seem to be of the same importance, with the effect of the amplitude modulation being prevalent. Furthermore, the overlap of the three conditional spectra suggests that the amount of frequency modulation is small in this region of the flow. This is consistent with the finding by Ganapathisubramani *et al.* (2012), their figure 8. If we then account for the effect of the local convection velocities, and introduce a horizontal shift, the three spectra diverge from each other. In figure 16(*b,d*), we observe the effect of this horizontal shift. Similarly to the near-wall region of the TBL, for the outer region it is also difficult to draw firm conclusions on the amplitude modulation, only on the basis of the conditional spectra. However, the divergence of the conditional spectra after the compensation suggests that the Taylor hypothesis leads to underestimation of the amplitude modulation in the outer region of a TBL, at the high frequencies of the interval. This warrants further investigation in the future.

To summarize, the effects of the local convection velocities in the conditional spectra as described in detail in §§ 6 and 9 have been compensated by applying a horizontal shift in frequency (figure 16). In the inner region of the TBL, the conditional spectra tend to collapse at the high frequencies mostly at scales smaller than the local Taylor length scale λ_T. This is evidence that the frequency modulation found in the near-wall region of a TBL (Ganapathisubramani *et al.* 2012, figure 8) occurs in time series and not in physical space. However, it is more difficult to interpret the implications that this effect can have on the amplitude modulation quantified in the literature as those including length scales up to δ in the small-scale signals. In the outer region of the TBL, the conditional spectra diverge after compensating for the local convection velocities, which could indicate that the amplitude modulation is underpredicted when converting from a time-frame into a space-frame. Nevertheless, further investigations based on PIV data at high resolution are required to quantify the amplitude modulation in a TBL, in physical space.

11. Conclusions

In the present work, amplitude and frequency modulation of the small scales of turbulence in a jet at high Reynolds number has been investigated experimentally using both HWA and PIV. Data were acquired at 70 nozzle diameters downstream from the nozzle, thus in the fully developed region. HWA time series were converted into space series after applying the Taylor hypothesis of frozen turbulence. By making use of a spectral filter, two signals were reconstructed from the original signal, one representative of the large scales (large-scale signal), and another representative of the small scales (small-scale signal). It was found that when the large-scale signal fluctuates positively, the small-scale signal is stronger in amplitude (amplitude modulation), and presents an increase in its number of local maxima and minima locally (frequency modulation). The opposite behaviour was found for negative fluctuations of the large-scale signal. The response of the small-scale motions to amplitude modulation can be considered instantaneous, being one Kolmogorov time scale. Moreover, the local standard deviation of the small-scale signal (representative of the amplitude of the small-scale signal) increases with the local strength of the

https://doi.org/10.1017/jfm.2015.227 Published online by Cambridge University Press

large-scale fluctuations, similar to the near-wall region of a TBL (Ganapathisubramani *et al.* 2012). The trend is linear for fluctuations of the large-scale signal of modest size, but is generally nonlinear.

Amplitude and frequency modulation was further investigated with long-range μPIV. The use of PIV permits spatial resolution of the small scale of turbulence without the need for the Taylor hypothesis of frozen turbulence. The size of the structures of intense vorticity conditioned on strongly positive and strongly negative large-scale fluctuations was examined. It was observed that the size of the structures of vorticity does not change significantly in relation to the large-scale velocity fluctuation, meaning that there is no significant spatial frequency modulation in PIV. The coherent structures of intense vorticity were found to be characterized statistically by velocities higher than the mean velocity of the flow. The structures of intense dissipation, which are located in close vicinity to the structures of vorticity (consistent with Ganapathisubramani *et al.* 2008), presented a similar trend. These findings led us to link amplitude modulation from PIV to the spatially inhomogeneous distribution of the coherent structures of vorticity and of intense dissipation. In particular, these coherent structures tend to be located in high-velocity regions of the flow.

The analysis from the PIV data shows that the amount of amplitude modulation is 25 % of the value measured with HWA. This overestimation of the amplitude modulation from hot-wire signals was attributed to application of the Taylor hypothesis of frozen turbulence in the analysis of hot-wire signals. In fact, the fixed spectral band filter used to obtain the large- and small-scale signals does not consider the local convection velocity, but rather the mean velocity of the flow. This leads to a different spatial frequency content within the same small-scale signal depending on the local strength of large-scale fluctuation. The conditional spectra overlap when a compensating shift is introduced based on the local convection velocity (approximated by the local strength of the large-scale fluctuation), which clarifies the effect of the Taylor hypothesis in estimating amplitude and frequency modulation from HWA. This effect has also been shown analytically in the paper. It must be noted that this overestimation of amplitude modulation in hot-wire time-series compared to the PIV data can also be interpreted physically as the difference between scale interactions in space and time. It seems that temporal interactions across scales are stronger and more active compared to the concurrent spatial interactions. This suggests that the comparison between amplitude modulation in space and in time must be carried out in different flows in order to highlight the differences in the interaction between spatial and temporal scales. To the best of our knowledge, this is the first and only study thus far to make this direct comparison. All previous studies utilize either time-series data (Bandyopadhyay & Hussain 1984; Mathis *et al.* 2009; Ganapathisubramani *et al.* 2012) or simply have PIV data (Buxton & Ganapathisubramani 2014).

Finally, the implications of the present findings to a TBL were explored. The evidence from the literature suggests that in the near wall the structures of vorticity present, on average, convection velocities higher than the local average velocity of the flow, whereas the opposite behaviour occurs in the outer region. Following our argument developed for jet flow, the frequency modulation found in Ganapathisubramani *et al.* (2012) is largely associated with varying convection velocities of the small scales (below a Taylor length). In the outer layer, the modulation of the high-frequency part of the small scales is underestimated when evaluated from velocity time-series.

https://doi.org/10.1017/jfm.2015.227 Published online by Cambridge University Press

Acknowledgements

B.G. acknowledges the support from the European Research Council under the European Union's Seventh Framework Programme (FP7/2007-2013), ERC grant agreement 277472.

REFERENCES

ADRIAN, R. J., MEINHART, C. D. & TOMKINS, C. D. 2000 Vortex organization in the outer region of the turbulent boundary layer. *J. Fluid Mech.* **422**, 1–54.

DEL ÁLAMO, J. C. & JIMÉNEZ, J. 2009 Estimation of turbulent convection velocities and corrections to Taylor's approximation. *J. Fluid Mech.* **640**, 5–26.

ASHURST, W. T., KERSTEIN, A. R., KERR, R. M. & GIBSON, C. H. 1987 Alignment of vorticity and scalar gradient with strain rate in simulated Navier–Stokes turbulence. *Phys. Fluids* **30**, 2343–2353.

BANDYOPADHYAY, P. R. & HUSSAIN, K. M. F. 1984 The coupling between scales in shear flows. *Phys. Fluids* **27**, 2221–2228.

BERNARDINI, M. & PIROZZOLI, S. 2011 Inner/outer layer interactions in turbulent boundary layers: a refined measure for the large-scale amplitude modulation mechanism. *Phys. Fluids* **23**, 061701.

BUXTON, O. R. H. 2011 Fine scale features of turbulent shear flows. PhD thesis, Imperial College London.

BUXTON, O. R. H. & GANAPATHISUBRAMANI, B. 2014 Concurrent scale interactions in the far-field of a turbulent mixing layer. *Phys. Fluids* **26**, 125106.

CARDESA, J. I., MISTRY, D., GAN, L. & DAWSON, J. R. 2013 Invariants of the reduced velocity gradient tensor in turbulent flows. *J. Fluid Mech.* **716**, 597–615.

CHACIN, J. M. & CANTWELL, B. J. 2000 Dynamics of a low Reynolds number turbulent boundary layer. *J. Fluid Mech.* **404**, 87–115.

CHUNG, D. & MCKEON, B. J. 2010 Large-eddy simulation of large-scale structures in long channel flow. *J. Fluid Mech.* **661**, 341–364.

ELSINGA, G. E., ADRIAN, R. J., VAN OUDHEUSDEN, B. W. & SCARANO, F. 2010 Three-dimensional vortex organization in a high-Reynolds-number supersonic turbulent boundary layer. *J. Fluid Mech.* **644**, 35–60.

ELSINGA, G. E. & MARUSIC, I. 2010 Universal aspects of small-scale motions in turbulence. *J. Fluid Mech.* **662**, 514–539.

FISCALETTI, D., ELSINGA, G. E., GANAPATHISUBRAMANI, B. & WESTERWEEL, J. 2013 Amplitude and frequency modulation of the small scales in a turbulent jet. In *8th International Symposium on Turbulence and Shear Flow Phenomena, 28–30 August, Poitiers*.

FISCALETTI, D., WESTERWEEL, J. & ELSINGA, G. E. 2014 Long-range μPIV to resolve the small scales in a jet at high Reynolds number. *Exp. Fluids* **55**, 1812.

GANAPATHISUBRAMANI, B., HUTCHINS, N., MONTY, J. P., CHUNG, D. & MARUSIC, I. 2012 Amplitude and frequency modulation in wall turbulence. *J. Fluid Mech.* **708**, 1–31.

GANAPATHISUBRAMANI, B., LAKSHMINARASIMHAN, K. & CLEMENS, N. T. 2008 Investigation of three-dimensional structure of fine scales in a turbulent jet by using cinematographic stereoscopic particle image velocimetry. *J. Fluid Mech.* **598**, 141–175.

HUTCHINS, N. & MARUSIC, I. 2007*a* Evidence of very long meandering features in the logarithmic region of turbulent boundary layers. *J. Fluid Mech.* **579**, 1–28.

HUTCHINS, N. & MARUSIC, I. 2007*b* Large-scale influences in near-wall turbulence. *Phil. Trans. R. Soc. Lond.* A **365**, 647–664.

ISHIHARA, T., KANEDA, Y. & HUNT, J. C. R. 2013 Thin shear layers in high Reynolds number turbulence: DNS results. *Flow Turbul. Combust.* **91**, 895–929.

ISHIHARA, T., TOSHIYUKI, G. & KANEDA, Y. 2009 Study of high-Reynolds number isotropic turbulence by direct numerical simulation. *Annu. Rev. Fluid Mech.* **41**, 165–180.

JACOBI, I. & MCKEON, B. J. 2013 Phase relationships between large and small scales in the turbulent boundary layer. *Exp. Fluids* **54**, 1481.

https://doi.org/10.1017/jfm.2015.227 Published online by Cambridge University Press

JIMÉNEZ, J. & PINELLI, A. 1999 The autonomous cycle of near-wall turbulence. *J. Fluid Mech.* **389**, 335–359.

JIMÉNEZ, J., WRAY, A. A., SAFFMAN, P. G. & ROGALLO, R. S. 1993 The structure of intense vorticity in isotropic turbulence. *J. Fluid Mech.* **225**, 65–90.

KANEDA, Y. & ISHIHARA, T. 2006 High-resolution direct numerical simulation of turbulence. *J. Turbul.* **7**, 1–17.

MARUSIC, I., MATHIS, R. & HUTCHINS, N. 2010 Predictive model for wall-bounded turbulent flow. *Science* **329**, 193–196.

MATHIS, R., HUTCHINS, N. & MARUSIC, I. 2009 Large-scale amplitude modulation of the small-scale structures in turbulent boundary layers. *J. Fluid Mech.* **628**, 311–337.

MATHIS, R., HUTCHINS, N. & MARUSIC, I. 2011 A predictive inner–outer model for streamwise turbulence statistics in wall-bounded flows. *J. Fluid Mech.* **681**, 537–566.

MATHIS, R., MARUSIC, I., HUTCHINS, N. & SREENIVASAN, K. R. 2011 The relationship between the velocity skewness and the amplitude modulation of the small scale by the large scale in turbulent boundary layers. *Phys. Fluids* **23**, 121702.

PANCHAPAKESAN, N. R. & LUMLEY, J. L. 1993 Turbulence measurements in axisymmetric jets of air and helium. Part 1. Air jet. *J. Fluid Mech.* **246**, 197–223.

POPE, S. B. 2000 *Turbulent Flows*. Cambridge University Press.

RICHARDSON, L. 1926 Atmospheric diffusion shown on a distance–neighbour graph. *Proc. R. Soc. Lond.* A **110**, 709–737.

SCHLATTER, P. & ÖRLÜ, R. 2010 Quantifying the interaction between large and small scales in wall-bounded turbulent flows: a note of caution. *Phys. Fluids* **22**, 051704.

SCHOPPA, W. & HUSSAIN, F. 2002 Coherent structure generation in near-wall turbulence. *J. Fluid Mech.* **453**, 57–108.

SHE, Z. S., JACKSON, E. & ORSZAG, S. A. 1990 Intermittent vortex structures in homogeneous isotropic turbulence. *Nature* **344**, 226–228.

SHEN, X. & WARHAFT, Z. 2000 The anisotropy of the small scale structure in high Reynolds number ($R_\lambda \sim 1000$) turbulent shear flow. *Phys. Fluids* **12**, 2976–2989.

SIGGIA, E. D. 1981 Numerical study of small-scale intermittency in three dimensional turbulence. *J. Fluid Mech.* **107**, 375–406.

SLOT, H. J., MOORE, P., DELFOS, R. & BOERSMA, B. J. 2009 Experiments on the flow field and acoustic properties of a Mach number 0.75 turbulent air jet at a low Reynolds number. *Flow Turbul. Combust.* **83**, 587–611.

SREENIVASAN, K. R. & ANTONIA, R. A. 1997 The phenomenology of small-scale turbulence. *Annu. Rev. Fluid Mech.* **29**, 435–472.

TAYLOR, G. I. 1935 Statistical theory of turbulence: parts I–III. *Proc. R. Soc. Lond.* A **151**, 421–464.

TAYLOR, G. I. 1938 The spectrum of turbulence. *Proc. R. Soc. Lond.* A **164**, 476–490.

VINCENT, A. & MENEGUZZI, M. 1991 The spatial structure and statistical properties of homogeneous turbulence. *J. Fluid Mech.* **225**, 1–20.

VINCENT, A. & MENEGUZZI, M. 1994 The dynamics of vorticity tubes in homogeneous turbulence. *J. Fluid Mech.* **258**, 245–254.

WEI, L., ELSINGA, G. E., BRETHOUWER, G., SCHLATTER, P. & JOHANSSON, A. V. 2014 Universality and scaling phenomenology of small-scale turbulence in wall-bounded flows. *Phys. Fluids* **26**, 035107.

WORTH, N. A. & NICKELS, T. B. 2011 Some characteristics of thin shear layers in homogeneous turbulent flow. *Phil. Trans. R. Soc. Lond.* A **369**, 709–722.

ZAMAN, K. B. M. Q. & HUSSAIN, A. K. M. F. 1981 Taylor hypothesis and large-scale coherent structures. *J. Fluid Mech.* **112**, 379–396.

ZHOU, J., ADRIAN, R. J., BALACHANDAR, S. & KENDALL, T. M. 1999 Mechanisms for generating coherent packets of hairpin vortices in channel flow. *J. Fluid Mech.* **387**, 353–396.

https://doi.org/10.1017/jfm.2015.227 Published online by Cambridge University Press